Ground-Based Radar Reflectivity Mosaic of Mei-yu Precipitation Systems over the Yangtze River–Huaihe River Basins

Yali LUO[*1,2], Weimiao QIAN[3], Yu GONG[4], Hongyan WANG[1], and Da-Lin ZHANG[1,5]

[1]*State Key Laboratory of Severe Weather, Chinese Academy of Meteorological Sciences, Beijing* 100081, *China*

[2]*Collaborative Innovation Center on Forecast and Evaluation of Meteorological Disasters,*
Nanjing University of Information Science & *Technology, Nanjing* 210044, *China*

[3]*Shijiazhuang Meteorological Bureau, Shijiazhuang* 050081, *China*

[4]*National Meteorological Center of China, Beijing* 100081, *China*

[5]*Department of Atmospheric and Oceanic Science, University of Maryland,*
College Park, Collage Park, Maryland 20742, *USA*

ABSTRACT

The 3D radar reflectivity produced by a mosaic software system, with measurements from 29 operational weather radars in the Yangtze River–Huaihe River Basins (YRHRB) during the mei-yu season of 2007, is compared to coincident TRMM PR observations in order to evaluate the value of the ground-based radar reflectivity mosaic in characterizing the 3D structures of mei-yu precipitation. Results show reasonable agreement in the composite radar reflectivity between the two datasets, with a correlation coefficient of 0.8 and a mean bias of −1 dB. The radar mosaic data at constant altitudes are reasonably consistent with the TRMM PR observations in the height range of 2–5 km, revealing essentially the same spatial distribution of radar echo and nearly identical histograms of reflectivity. However, at altitudes above 5 km, the mosaic data overestimate reflectivity and have slower decreasing rates with height compared to the TRMM PR observations. The areas of convective and stratiform precipitation, based on the mosaic reflectivity distribution at 3-km altitude, are highly correlated with the corresponding regions in the TRMM products, with correlation coefficients of 0.92 and 0.97 and mean relative differences of −7.9% and −2.5%, respectively. Finally, the usefulness of the mosaic reflectivity at 3-km altitude at 6-min intervals is illustrated using a mesoscale convective system that occurred over the YRHRB.

Key words: ground-based radar reflectivity mosaic, mei-yu precipitation, mesoscale convective system, TRMM PR

---

1. Introduction

Radar reflectivity observations have been widely used in meteorological studies, mainly to characterize heavy-rain-producing and/or damage-causing mesoscale convective systems (MCSs). Composite radar reflectivity (i.e., the horizontal distribution of maximum radar reflectivity in columns, or "CR" for short) has been used in numerous studies to define and investigate linear MCSs at a variety of locations over the world, such as the Taiwan Strait and western Taiwan (Chen and Chou, 1993), the southeastern United States (Geerts, 1998), the central United States (Parker and Johnson, 2000), and mainland China (Meng and Zhang, 2012). Algorithms have been developed to partition the radar echoes into convective and stratiform regions (e.g., Steiner et al., 1995) and have been extensively applied to characterizing precipitation systems (e.g., Cifelli et al., 2007). Vertical profiles of radar reflectivity (VPRR) have been compared between mid-latitude continental, tropical continental, and tropical oceanic MCSs (Zipser and Lutz, 1994). Substantial differences in the VPRR characteristics have been noticed among the three MCS classes, linked to differences in the strength of up-drafts within the MCSs and to storm electrification (Zipser and Lutz, 1994). Reflectivity from the TRMM (Simpson et al., 1996) PR (Kawanishi et al., 2000) has also been used to examine 3D structures of summer monsoonal convection in the Himalayan region and its overall variability (Houze et al., 2007). Moreover, the maximum height of 30 dBZ, the maximum reflectivity at 6-km altitude above sea level (ASL), and VPRR based on TRMM PR observations, have been analyzed to study mesoscale properties of East Asian monsoonal pre-

---
* Corresponding author: Yali LUO

  Email: yali@camscma.cn

cipitation systems (Xu et al., 2009; Luo et al., 2013b). These studies have provided valuable guidance for MCS operational forecasting.

Heavy rainfall occurs frequently over the highly populated Yangtze River–Huaihe River Basins (YRHRB; rectangular box in Fig. 1) during the mei-yu season (climatologically from mid-June to mid-July), which is one of three heavy-rainfall periods in China formed in close association with the northward march of the East Asian summer monsoon (Ding, 1992; Ding and Chan, 2005). China started construction of a Doppler radar network in 1998 as a 10-yr program, and 112 radars were operational in 2007, including 29 radars around the YRHRB. These radars are the same as the Weather Surveillance Radar units in the United States, i.e., they are powerful 10-cm wavelength radars with a beam width of approximately $1°$, a 1-km range resolution, and a volume scan sampling frequency of approximately 6 min. Each volume scan consists of nine sweeps, with elevation angles ranging from $0.5°$ (base scan) to $19°$. With an effective scan radius of approximately 150 km, the radars almost completely cover the entire YRHRB region, which mostly consists of flat land (Fig. 1).

A 3D multi-radar mosaic software system has been developed at the State Key Laboratory of Severe Weather of the Chinese Academy of Meteorological Sciences (Wang et al., 2009). The system removes ground clutter from the raw data using a fuzzy logic method (Kessinger et al., 2003; Liu et al., 2008). The 3D spherical data from each radar are then converted to a 3D Cartesian coordinate system using the nearest neighbor in range and azimuth directions and linear interpolations between the elevation angles. Finally, all the data are integrated to cover the full analysis region. For locations covered by multiple radars, an exponential weighting function of the distance between the radar and the target place is used to take into account the measurements from multiple radars (Zhang et al., 2005; Langston et al., 2007). The grid spacing of the radar mosaic is $0.01°$ (i.e., about 1 km) in the hori-

zontal and varies in the vertical (500 m below 6-km altitude ASL, 1 km at 6–20-km altitudes). It should be noted that it is the radar sampling resolution, not the grid spacing, that determines the resolvable storm structure. The 3D mosaic reflectivity minimizes the inherent limitation of single radars, such as their small coverage, cone of silence, and misdetection of precipitation echoes at lower elevation due to Earth's curvature. The 3D mosaic data can potentially reveal the rapid evolution of fine-scale structures of precipitation systems because of their high resolution relative to conventional observations, as demonstrated in case studies (e.g., Luo et al., 2010, 2013a). The data can be applied to studying precipitation climatology, as they cover a large area and long periods of time. Moreover, the data can be directly compared to model outputs, and conveniently co-analyzed with other observational data sources (e.g., satellite data), as they are produced on 3D gridded coordinates. In short, the 3D mosaic reflectivity data from the radar network over the YRHRB are potentially very valuable for detailed case studies and climatological studies on East Asian monsoonal precipitation, as well as the evaluation of regional NWP and climate models.

However, the 3D reflectivity mosaic data from the radar network in the YRHRB may have certain limitations, due to uncertainties associated with calibration bias, sparse sampling of the radar scan at higher altitudes, different attenuation, and different beam blockage. These limitations are unknown to many potential users of the 3D reflectivity mosaic data, since they have not been systematically evaluated, but are nevertheless important because of the data's meaningful application in the aforementioned research areas.

Thus, in the present study, we seek to address this knowledge gap by clarifying the applicability and limitations of the 3D mosaic reflectivity from China's radar network over the YRHRB region. Whereas numerous studies have employed TRMM PR observations to calibrate ground-based radars (GRs) at various locations over the world (Bolen and Chandrasekar, 2000; Heymsfield et al., 2000; Schumacher
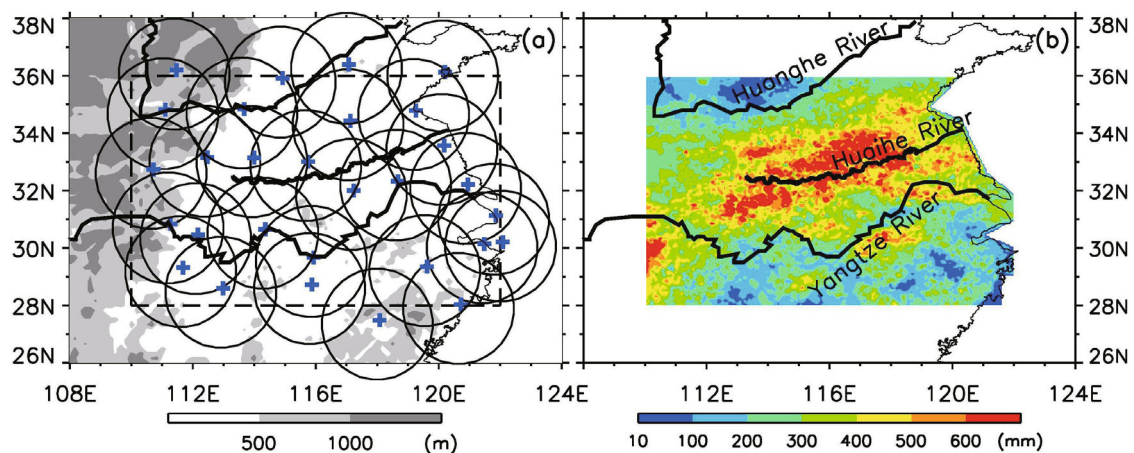

Fig. 1. (a) Distribution of radars (blue crosses) over the YRHRB, in which their coverage is represented by circles of a 150-km radius. Shading denotes the terrain height (units: m). The rectangular box (dashed) denotes the YRHRB defined in the present study. (b) Accumulated precipitation (units: mm) during the 2007 mei-yu season (19 June to 26 July 2007). The thick black lines denote the Huaihe, Yangtze and Huanghe rivers, and the thin black lines represent the coastline.

and Houze, 2000; Anagnostou et al., 2001; Liao et al., 2001; Houze et al., 2004; Wang and Wolff, 2009), the present study attempts to answer the following questions by matching and comparing the mosaic reflectivity with TRMM PR observations using a similar comparison approach: Is the composite radar reflectivity from the 3D mosaic data reasonably accurate? To what extent can the 3D mosaic data be used to describe the vertical structures of the mei-yu precipitation? Can we obtain reasonable partitioning between convective and stratiform precipitation by applying the partitioning algorithm of Steiner et al. (1995) to the mosaic data?

The next section describes the data and methodology used in the present study. Section 3 qualitatively compares the mosaic data to reflectivity from TRMM PR observations. Section 4 presents a comprehensive comparison between the two data sources in terms of the composite radar reflectivity, radar reflectivity at constant altitudes, and partitioning between convective and stratiform precipitation regions. Section 5 demonstrates the quality of the mosaic data through an example of application to the evolution of an MCS along a mei-yu front. A summary and conclusions are given in the final section.

2. Data and methodology

To evaluate the quality of the 3D mosaic reflectivity, we compare the data to coincident TRMM PR observations (Kummerow et al., 1998) over the YRHRB region during the mei-yu season of 2007, after matching the two datasets onto a common Earth parallel 3D grid. The PR onboard TRMM has a 13.8-GHz frequency (2.2-cm wavelength), a field-of-view diameter of about 5.0 km (after a boost in August 2001) at nadir, a 0.25-km range resolution, and a nominal sensitivity of approximately 17 dBZ (Simpson et al., 1996). Both internal and external calibrations of the PR have been performed to ensure accurate and stable rain measurements. Both calibrations have shown that the PR is able to consistently measure reflectivity with absolute calibration accuracy better than ±1 dB (Kozu and Iguchi, 1999; Kawanishi et al., 2000; Takahashi et al., 2003). PR reflectivity observations have thus served as a consistent reference to calibrate GRs and detect inconsistencies between adjacent GRs (Schumacher and Houze, 2000; Anagnostou et al., 2001; Houze et al., 2004; Wang and Wolff, 2009; Zhu et al., 2016).

The mei-yu season undergoes substantial interannual variation (Luo et al., 2013b), and the year of 2007 featured a prolonged mei-yu season from 19 June to 26 July (Zhao et al., 2007). The occurrence of torrential rainfall exceeding 600 mm during the 2007 mei-yu season (Fig. 1b) generated the worst flood events over the Huaihe River valley since 1954, causing tremendous economic loss and leaving more than 10 million people without a home. During the 2007 mei-yu season, there were 117 TRMM overpasses, each of which scanned at least 50 rainy pixels over the YRHRB region, where a rainy pixel is defined as a PR pixel with the maximum radar reflectivity in the column of ⩾18 dBZ.

The total number of rainy pixels was 161 404, accounting for 11% of the total (rainy plus non-rainy) pixels over the region during the period. These PR profiles are composed of attenuation-corrected reflectivity for each PR scan ray (Iguchi et al., 2000).

Temporal and spatial matching between the 3D mosaic reflectivity and the attenuation-corrected PR reflectivity profiles (TRMM 2A25) (TRMM PR Team, 2011) was performed to allow for reasonable comparisons. First, the mosaic reflectivities that were the closest in time to the 117 TRMM overpasses over the YRHRB, and located within the TRMM tracks, were resampled. The TRMM satellite flies over the analysis region within 1–3 min during each overpass. Each PR scan only lasts about 0.6 s, whereas the GR volume scan lasts about 6 min. Consequently, the PR and mosaic data can be off in time by ~6 min at most. Second, the simultaneous mosaic reflectivity and TRMM PR data were interpolated to the same grid with the lower resolution of the two datasets, i.e., the same resolution as TRMM PR in the horizontal direction, and the same as the mosaic data in the vertical direction. We averaged the linear reflectivity to avoid averaging biases associated with the logarithmic reflectivity (dBZ) calculations. The linear averaging was performed in both the horizontal direction (for the mosaic reflectivity) and vertical direction (for TRMM 2A25) for consistency. Once the averaging was complete, linear units were converted back to logarithmic ones. This matching scheme can minimize uncertainties associated with the sampling resolution differences between the GR and PR. The matching scheme is similar to other schemes presented in the literature (e.g., Heymsfield et al., 2000; Anagnostou et al., 2001; Liao et al., 2001; Wang and Wolff, 2009), regardless of the detailed technical differences among these studies. The matched gridded reflectivities from the TRMM PR observations and mosaic data were then compared, both qualitatively and quantitatively, as described in the following sections.

Numerous studies have partitioned convective and stratiform precipitation (Houze, 1997) and contrasted their characteristics, such as their temporal and geographical distributions (e.g., Cifelli et al., 2007). In the present study, the convective and stratiform partitioning algorithm of Steiner et al. (1995) was applied to the mosaic reflectivity, and the results (e.g., areas of convective/stratiform precipitation) compared to those in the TRMM PR 2A23 product (Funk et al., 2013). The algorithm of Steiner et al. (1995) partitions the convective and stratiform regions on the basis of the intensity and sharpness of the peak echo intensity at 3-km altitude ASL. Detailed information about the TRMM algorithms and products can be found in the Version 7 PR manual (TRMM PR Team, 2011).

3. Qualitative comparison between mosaic and TRMM PR reflectivity

In this section, we qualitatively compare the mosaic to the TRMM PR reflectivity by visual inspection of the distri-

butions at a constant altitude (i.e., 3 km ASL) and in vertical cross sections. For this purpose, Fig. 2 shows three examples of reflectivity distributions at 3-km altitude ASL from the TRMM PR and mosaic data, with rainy regions being detected on 5, 6 and 9 July 2007 to the north, along and to the south of the Huaihe River, respectively. At each time instant, the horizontal distributions of radar reflectivity from the two datasets present essentially the same features in terms of the spatial pattern of MCSs (linear or scattered) and the locations of precipitation centers, despite some minor differences in detailed structures and intensities.

Figure 3 presents another example of not only horizontal distributions but also vertical cross sections of reflectivity at about 2024 UTC 18 July 2007. Both datasets reveal the presence of a banded precipitation region extending northeastward from near the upper reaches of the Huaihe River to the ocean (Figs. 3a and c). The linear MCS consists of a few localized convective cells to the west, a small area of intense convective echoes to the southwest, and a major one to the northeast, embedded within a broad stratiform precipitation region. Vertical cross sections were selected inside the rainy system, along which both datasets show continuous echoes with distinct features (Figs. 3b and d). At the southwest end of the cross section in Fig. 3b, there are convective regions with echo tops extending up to 16 km and maximum reflectivity exceeding 50 dBZ; within 118.4°–119.2°E, there are some weaker convective cells with tops decreasing to 6–9-km altitude; and to the east of 119.2°E, there is a broader flat-topped precipitation region that contains a shallow bright band near 5-km altitude, which is seemingly the melting level. The vertical cross section from the GR mosaic (Fig. 3d) also exhibits deeper convective echoes to the southwest, lower-topped convective cells in the middle, and a broader weak reflectivity region to the east, i.e., qualitatively consistent with the TRMM data. However, the mosaic shows a relatively higher vertical extent of the MCS, slower decreasing rate of radar reflectivity above 5.5-km altitude, and no bright band near the 0°C level (near 5.5 km) in the northeastern portion of the cross section.
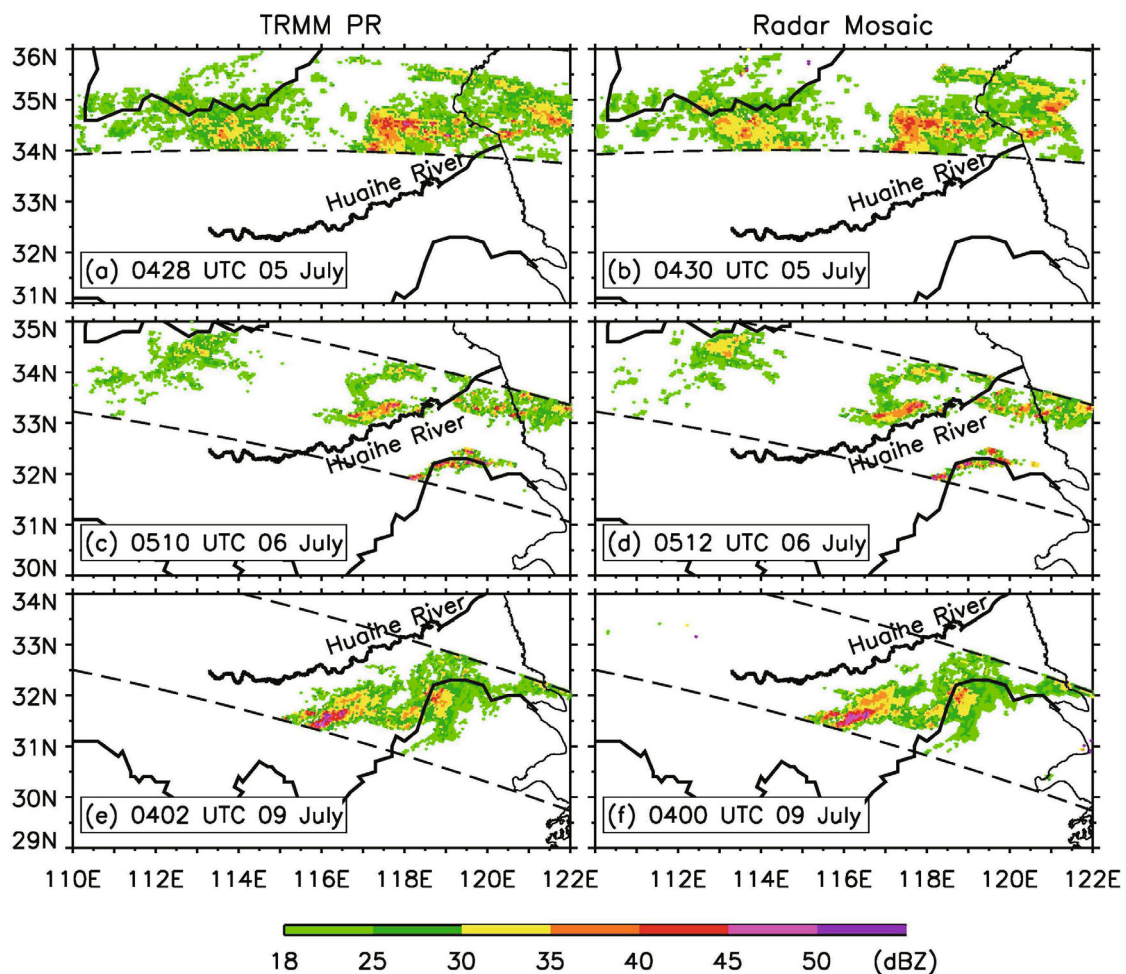

Fig. 2. Longitude–latitude distributions of radar reflectivity (units: dBZ) at 3-km altitude ASL from (a, c, e) the TRMM PR observations and (b, d, f) the GR mosaic, at selected times in 2007. The dashed lines represent the boundaries of the TRMM satellite's pathway at the surface, outside of which the mosaic reflectivity is not shown. Note the different latitude ranges among the top, middle and bottom panels, used to better illustrate the distributions of radar reflectivity at the individual times.
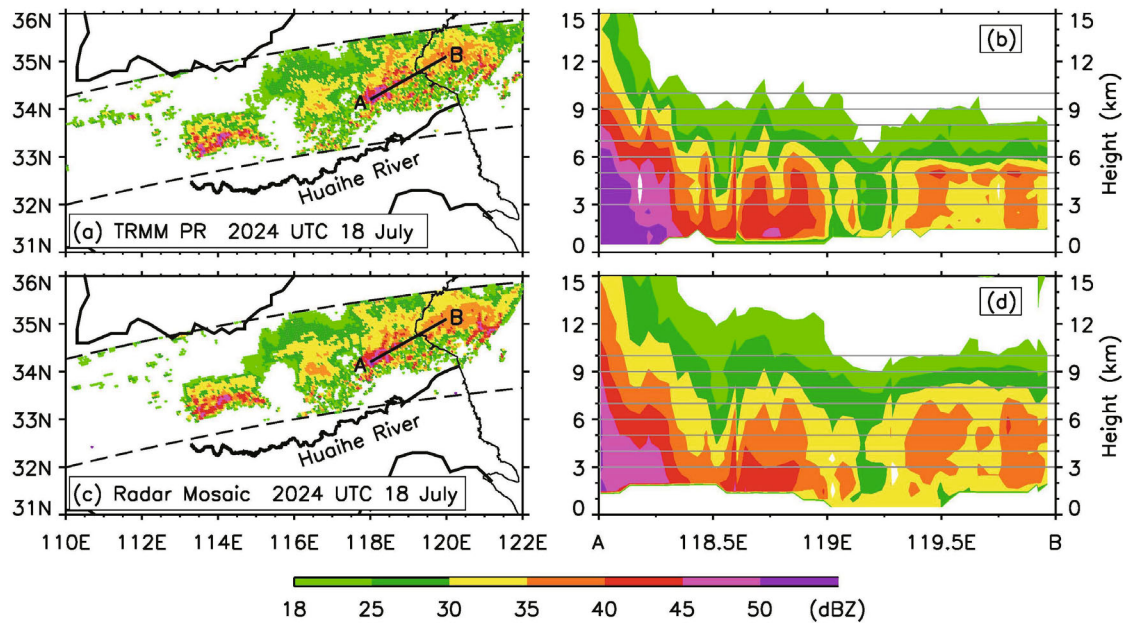
Fig. 3. (a, c) Longitude–latitude distributions of the matched gridded radar reflectivity (units: dBZ) at 3-km altitude ASL at 2014 UTC 18 July 2007: (a) TRMM PR observations; (c) mosaic reflectivity. The dashed lines represent the boundaries of the TRMM satellite's pathway at the surface, outside of which the mosaic reflectivity is not shown. (b, d) Vertical cross sections of the corresponding radar reflectivity along lines A–B in (a, c). The gray lines in (b, d) represent the constant altitudes ranging from 3 km to 10 km at 1-km intervals.

Statistical analysis was conducted to further corroborate this view, as reported upon in section 4.2.

4. Quantitative comparison between mosaic and TRMM PR reflectivity

In this section, we quantitatively compare the CR, radar reflectivity at constant altitudes, and the partitioning of convective and stratiform precipitation between the mosaic and TRMM PR data.

4.1. *Composite radar reflectivity*

Quantitative comparisons of CR between the two datasets were performed by analyzing the PDF (i.e., histogram), statistics of the CR difference at each grid, and correlation between the two data sources. Figure 4a shows that the two CR histograms agree reasonably well with one another, with a correlation coefficient of 0.8. The two distributions both increase sharply from 18 to 26 dBZ, reach a broad peak around 26–32 dBZ, and then decrease gradually with increasing CR. A major difference is that the mosaic CR has more weak echoes (i.e., <22 dBZ) than the TRMM PR CR, which is also reflected in the PDF of the CR difference (i.e., mosaic minus PR, in dB) (Fig. 4b). The CR difference presents a nonnormal feature, with a mean bias of −1.09 dB and a standard deviation of 4.14 dB. Two factors that have an adverse effect on the quality of the mosaic data could have contributed to this difference: one is the calibration error associated with individual radars, and the other is uncertainty in the method

used to merge the reflectivity observations in the area covered by multiple radars. Nevertheless, the majority (90%) of the differences are located between −4 dB and 3 dB.

4.2. *Radar reflectivity at constant altitudes*

Figure 5 compares the histograms of radar reflectivity at constant altitudes ranging from 2 km to 10 km between the TRMM PR and matched mosaic data. The two histograms at the lower altitudes (2–5 km) are nearly identical, with large corresponding correlation coefficients of 0.75–0.79, suggesting very good agreement between the two data sources. However, larger discrepancies are present at the higher altitudes. Peaks of the mosaic reflectivity distributions are shifted significantly toward the larger values compared to the TRMM PR observations, suggesting a substantial overestimation of reflectivity by the mosaic data above 5 km. This is consistent with the above visual comparison between the vertical cross sections in Figs. 3b and d. For example, the distribution of the TRMM PR reflectivity at 10-km altitude has a peak of 0.32 in the smallest bin (18–20 dBZ), whereas the peak in the mosaic data is much lower (i.e., 0.23), with its bin shifted to the 22–24 dBZ range. The correlation coefficients at the higher altitudes, ranging between 0.54 and 0.71, are also much smaller than those at the lower altitudes.

Figure 6 shows histograms of the reflectivity differences between the mosaic and TRMM PR data at the same altitudes as those shown in Fig. 5. The reflectivity difference field at 2–5-km altitudes exhibits a pronounced peak frequency at 0 dB, which decreases sharply toward larger and smaller
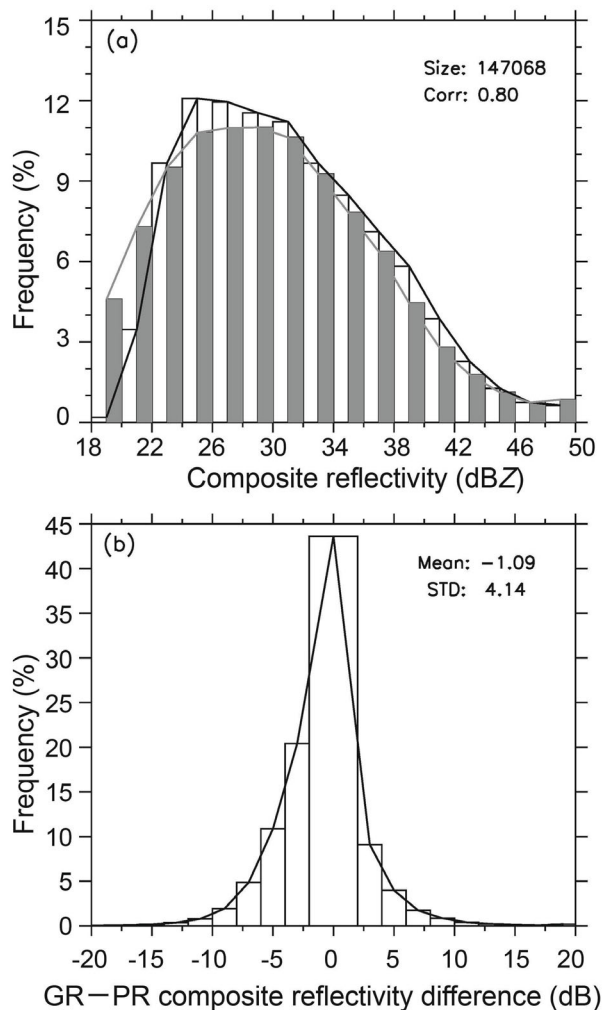
Fig. 4. (a) Histograms (units: %) of CR (units: dBZ) from the GR mosaic (gray line and bar) and the TRMM PR observations (black line and bar), with the number of samples and correlation coefficient indicated in the top-right corner of the panel. (b) Histogram of the CR difference (i.e., GR−PR), with the mean (units: dB) and standard deviation indicated in the top-right of the panel.

values, respectively, with absolute biases of less than 1 dB and standard deviations of about 4 dB. In contrast, the frequency distributions at higher altitudes broaden toward larger positive values, reflecting the overestimation of reflectivity in the mosaic data. This overestimation may be attributable to the following two factors: one is the insufficient sampling (i.e., the presence of gaps between scan elevations); and the other is the coarser resolution of the GR scans at higher altitudes as the beam width increases with distance. Based on the above comparison, we are able to conclude that the mosaic data at 2–5-km ASL altitudes are high quality, whereas those above the 5-km altitude should be used with caution. Therefore, the mosaic reflectivity could be used to reveal the vertical distribution of radar reflectivity as a measure of convective intensity, but only within a limited height range (e.g., 2–5 km ASL).

4.3. *Partitioning between convective and stratiform precipitation*

As mentioned in section 2, we partitioned the convective and stratiform precipitation in the GR reflectivity mosaic by applying the precipitation partitioning technique of Steiner et al. (1995). We then visually compared their spatial distributions to the corresponding ones in the TRMM PR 2A23 data during the 117 TRMM satellite overpasses over the YRHRB, and favorable agreement was found. As examples, Fig. 7 shows the spatial distributions of a number of convective and stratiform precipitation regions from TRMM 2A23, along with our estimation at approximately the same times as those shown in Fig. 2, on 5, 6 and 9 July 2007. One can clearly see that the two datasets are basically consistent with one another. Quantitative agreement was also obtained by statistically comparing the areas of convective and stratiform precipitation during the 2007 mei-yu season between the two datasets. Table 1 lists the correlation coefficients, mean differences, and mean relative differences (i.e., divided by TRMM 2A23's areas of each precipitation type), showing that the convective and stratiform precipitation areas between the two datasets are highly correlated (i.e., 0.92 and 0.97, respectively) and have small relative differences (i.e., −7.9% and −2.5%, respectively). The differences in the precipitation areas may be attributable to the differences between the two datasets (TRMM 2A25 and mosaic data), as well as between the different partitioning algorithms. Specifically, the TRMM 2A23 algorithm (Funk et al., 2013) determines each rainy pixel's classification first vertically and then horizontally using the method employed by Steiner et al. (1995), whereas we applied only the horizontal pixel classification method to the mosaic data without vertical classification.

5. Example of a high-resolution description of an MCS

Both the quantitative and the qualitative comparisons made in the preceding two sections reveal reasonable agreements between the mosaic reflectivity in the 2–5 km layer and the attenuation-corrected TRMM PR observations. In this section, we illustrate the great value of the mosaic reflectivity at 6-min intervals in helping examine the fine-scale evolutionary features of MCSs. For this purpose, an MCS, which developed over the Huaihe River basin in the early hours of 8 July 2007, was selected as an example of the heavy-rain-producing storms during the mei-yu season. Figure 8 shows the temporal evolution of radar reflectivity at 3 km ASL

Table 1. Statistics regarding the areas of convective and stratiform precipitation, determined using the mosaic reflectivity, in comparison with the TRMM 2A23 product.

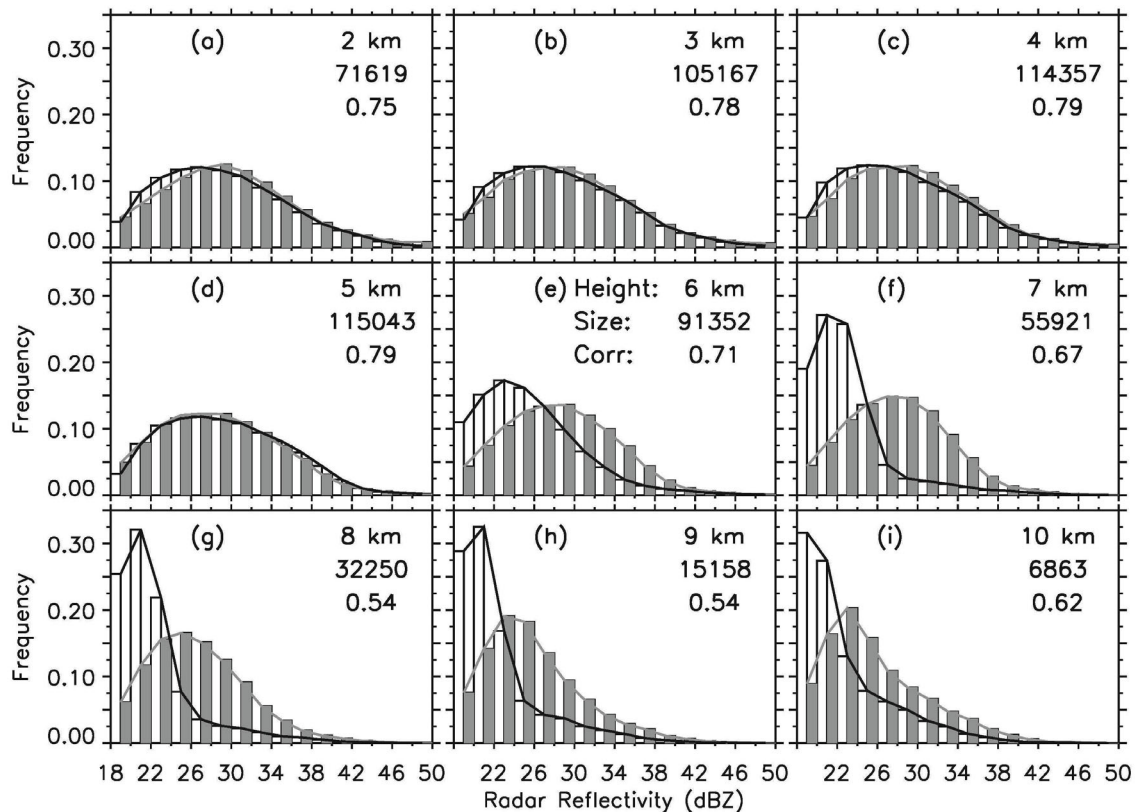| Precipitation type	Correlation coefficient	Mean difference (km²)	Relative difference (%)
Convective	0.92	−253.5	−7.9%
Stratiform	0.97	−2430.0	−2.5%

Fig. 5. Histograms (units: %) of the matched radar reflectivity (units: dBZ) at selected altitudes ranging from 2 km to 10 km derived from the TRMM PR observations (black line and white bar) and the GR mosaic (gray line and gray bar). The altitude (units: km), number of samples, and correlation coefficient are given in the top-right corner of each panel (top to bottom, respectively).

derived from the mosaic data at 24 selected times during a period of 11 hours, i.e., from 0000 to 1106 LST (Beijing Standard Time, UTC+8) 8 July 2007. It should be mentioned that Luo et al. (2014) studied the evolution of this MCS case using the mosaic reflectivity data, but with a lower temporal resolution, together with its associated model simulation. One can see that the MCS of concern was initiated near midnight and developed into a quasi-linear system consisting of numerous west–east or southwest–northeast oriented, band-shaped precipitation regions of reflectivity greater than 35 dBZ, hereafter simply referred to as rainbands. The major rainbands of interest in Fig. 8 could be traced from the 6-min resolution reflectivity and labeled sequentially in accordance with the time of their first appearances, following Luo et al. (2014).

Several notable features of importance to the growth and maintenance of the rainbands are described briefly as follows. First of all, the life cycles of many rainbands can be clearly traced from their first birth places and times, even as convective cells, to their final demise. As an example, a long-lived convective element of the MCS, i.e., rainband 1, is used herein to demonstrate the applicability of the mosaic reflectivity data to the detailed analysis of the structural evolution of a meso-β-scale convective system. Rainband 1 appeared first as a small convective band across the Huaihe River at (32.4°N, 115.4°E) at 0000 LST 8 July (Fig. 8a), and it grew

into an intense rainband at 0430 LST as it moved eastward along both the Huaihe River and the leading convective line of the MCS (Fig. 8j). It began weakening as it shifted to a southeastward movement at 0624 LST (Fig. 8o), and became mostly stratiform at 0906 LST (Fig. 8u). Interestingly, however, it re-intensified somehow at 1106 LST (Fig. 8x), and still remained traceable for another 2–3 hours after moving out of the study domain (not shown). This rainband also changed its orientation from west–east to west-northwest–east-southeast as it propagated over a distance of about 350 km during the previous 11-hour period. Such an analysis of high-resolution spatial and temporal data is indeed encouraging, because not only can it help reveal the detailed processes leading to the development of heavy-rain-producing MCSs, but also facilitate the validation of NWP models. In fact, Luo et al. (2014) develop a conceptual model of the associated heavy rainfall event, based on this dataset and model simulation, in which the echo- and rainband-training processes were identified.

Second, new convective cells can be seen to have repeatedly formed upstream of their predecessors and passed along the same path. That is, it was the backbuilding and echo-training process (Schumacher and Johnson, 2005, 2006; Luo et al., 2014) that led to the linear growth of the rainbands in extent. This phenomenon was most obvious during the early
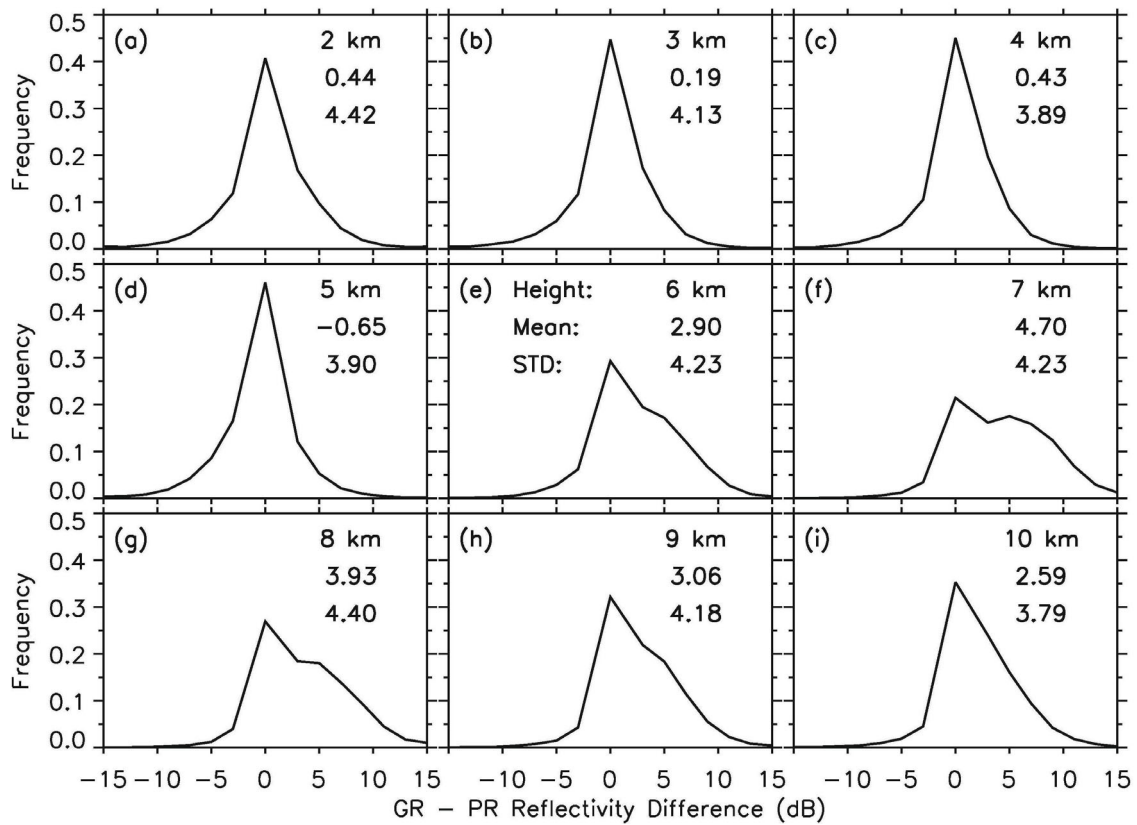
Fig. 6. Histograms (unit: %) of the radar reflectivity difference, i.e., mosaic reflectivity minus TRMM PR observations (units: dB). The altitude (units: km), mean (units: dB), and standard deviation are given in the top-right of each panel (top to bottom, respectively).
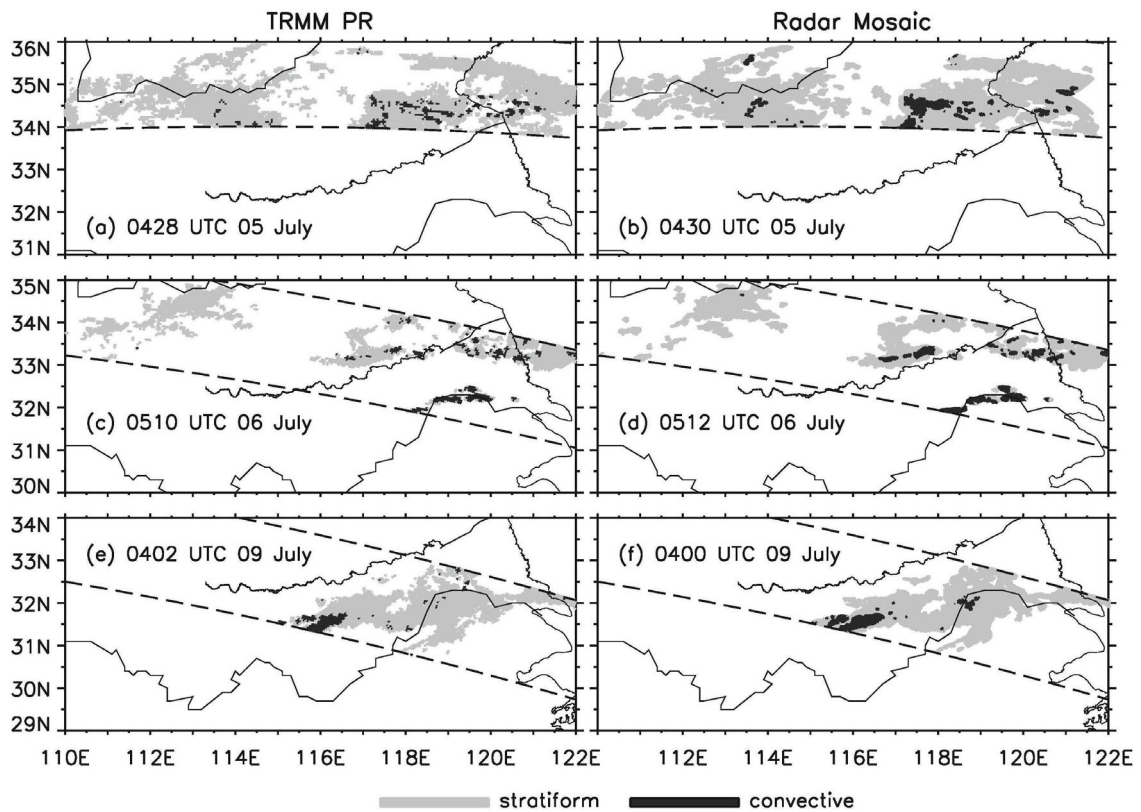

Fig. 7. As in Fig. 2, except for the distributions of stratiform and convective precipitation from (a, c, e) the TRMM PR observations and (b, d, f) the GR mosaic, at three selected times in July 2007.
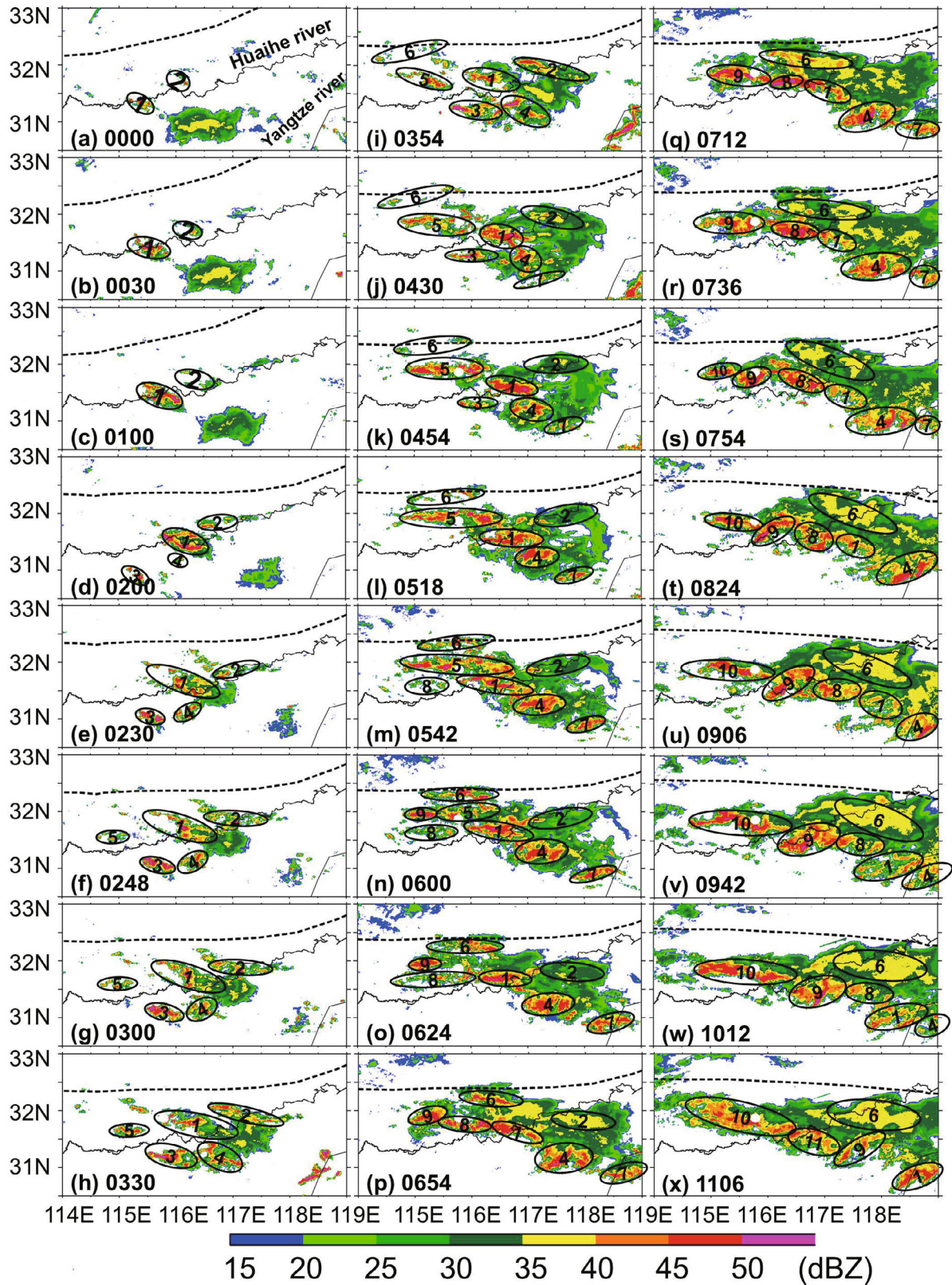
Fig. 8. Radar reflectivity (units: dBZ) at 3-km altitude ASL derived from the mosaic reflectivity at 24 selected times. The numbers (1–11) inside the ellipses are used to trace the evolution of the major rainbands. The dashed lines show the approximate position of the mei-yu front, as represented by the $\theta_e = 345$ K contour at 850 hPa estimated from ERA-Interim data (Dee et al., 2011), from which θ_e decreases northward. The ERA-Interim data at 0000, 0600, 1200 and 1800 LST 8 July 2007 are linearly interpolated in time to obtain the θ_e contours.

development stage of the MCS (e.g., rainbands 1–6 in Figs. 8a–m) and also in the western portion of the MCS during its later stage (e.g., rainband 10 in Figs. 8s–x). Moreover, the southeastward movement of these rainbands, referred to as "band training" by Luo et al. (2014), assisted the maintenance of the linear MCS under study.

Third, the formation of weaker (stratiform) precipitation regions between the convective rainbands and the mei-yu front can be seen to have resulted from the dissipation of rainbands 2 (Fig. 8j–o) and 6 (Fig. 8q–x) after they moved to the rear portion of the quasi-linear MCS and obtained less energy supply. Thus, the origin of this stratiform precipitation region differs from the trailing stratiform region in the conceptual model of a midlatitude mature squall line by Houze et al. (1989), and that in a model-simulated one (Zhang and Gao, 1989). The formation of the trailing stratiform region in their conceptual model and model simulation was mainly attributed to the detrainment of hydrometeors and buoyant air from the convective regions.

6. Summary and conclusions

In this study, simultaneous comparisons between the GR mosaic over central-eastern China and the attenuation-corrected TRMM PR observations during the mei-yu season of 2007 were conducted. The major findings can be summarized as follows:

The composite radar reflectivity is reasonably consistent between the two datasets, with a correlation coefficient of 0.8 and a bias of −1 dB. The differences are mostly (90%) between −4 dB and 3 dB. Partitioning between the convective and stratiform precipitation regions compares favorably between the two datasets: the corresponding correlation coefficients are 0.92 and 0.97 and the relative differences of the precipitation areas are −7.9% and −2.5% for convective and stratiform precipitation, respectively.

Histograms of the two datasets at constant altitudes from 2 to 5 km ASL are nearly identical, with correlation coefficients of 0.75–0.79. In contrast, at higher altitudes (i.e., 6–10 km ASL), peaks of the mosaic reflectivity distributions are shifted toward larger values relative to those in the TRMM PR observations and the correlation coefficients reduce to 0.54–0.71. The overestimation of the mosaic reflectivity at the higher altitudes may have resulted from insufficient samplings and the coarser resolution of the ground radar scans at the higher altitudes, and perhaps also by uncertainties associated with the mosaic software. Although the PR data are probably less reliable below the bright band (about 5 km in the mei-yu season), due to potential PR attenuation correction errors, numerous studies have shown that the TRMM PR is able to consistently measure reflectivity with absolute calibration accuracy better than ±1 dB (Kozu and Iguchi, 1999; Kawanishi et al., 2000; Takahashi et al., 2003). Therefore, the agreement between the mosaic reflectivity and the PR attenuation-corrected reflectivities at approximately 2–5 km ASL obtained in the present study supports the usefulness of

the mosaic reflectivity over the YRHRB in this height range, which is further demonstrated by showing the evolution of a heavy-rain-producing MCS with the mosaic reflectivity at 3-km altitude at 6-min intervals.

In conclusion, we have found that the composite reflectivity, radar reflectivity in the height range of 2–5 km ASL, and the partitioned convective and stratiform precipitation regions, based on the high-resolution GR reflectivity mosaic, can be used to characterize the 3D structures and evolution of precipitating systems over the YRHRB during the mei-yu season with reasonable accuracy. While the space-borne radars of TRMM and the Global Precipitation Measurement Mission (Hou et al., 2014) offer a glimpse into the internal vertical structures of precipitating systems in eastern China only twice per day, the radar reflectivity mosaic data can be used to reveal the details of MCS evolution at 6-min intervals.

However, caution should be exercised to interpret our results in the proper context, for a few reasons. First, the GRs over the YRHRB have not been calibrated to a certain standard, although observations below the bright band height from the radar at Nanjing have been analyzed and corrected by Zhu et al. (2016). Possible uncertainties associated with the data from individual ground radars could add uncertainty to the mosaic. Second, details of the methodology to construct the radar mosaic, such as the interpolation method and weighting function, need to be carefully investigated and refined to clarify/minimize their influences on the quality of the mosaic reflectivity. Moreover, evaluation for a longer period (3–5 years) is needed in order to draw more solid conclusions.

REFERENCES

Anagnostou, E. N., C. A. Morales, and T. Dinku, 2001: The use of TRMM precipitation radar observations in determining ground radar calibration biases. *J. Atmos. Oceanic Technol.*, **18**(4), 616–628.

Bolen, S. M., and V. Chandrasekar, 2000: Quantitative cross validation of space-based and ground-based radar observations. *J. Appl. Meteor.*, **39**, 2071–2079.

Chen, G. T. J., and H. C. Chou, 1993: General characteristics of squall lines observed in TAMEX. *Mon. Wea. Rev.*, **121**(3), 726–733.

Cifelli, R., S. W. Nesbitt, S. A. Rutledge, W. A. Petersen, and S. Yuter, 2007: Radar characteristics of precipitation features in the EPIC and TEPPS regions of the east Pacific. *Mon. Wea. Rev.*, **135**(4), 1576–1595.

Dee, D. P., and Coauthors, 2011: The ERA-Interim reanalysis: Configuration and performance of the data assimilation system. *Quart. J. Roy. Meteor. Soc.*, **137**(656), 553–597.

Ding, Y. H., 1992: Summer monsoon rainfalls in China. *J. Meteor. Soc. Japan*, **70**(1B), 373–396.

Ding, Y. H., and J. C. L. Chan, 2005: The East Asian summer monsoon: An overview. *Meteor. Atmos. Phys.*, **89**(1–4), 117–142.

Funk, A., C. Schumacher, and J. Awaka, 2013: Analysis of rain classifications over the tropics by version 7 of the TRMM PR 2A23 algorithm. *J. Meteor. Soc. Japan*, **91**(3), 257–272.

Geerts, B., 1998: Mesoscale convective systems in the southeast United States during 1994–95: A survey. *Wea. Forecasting*, **13**(3), 860–869.

Heymsfield, G. M., B. Geerts, and L. Tian, 2000: TRMM precipitation radar reflectivity profiles as compared with high-resolution airborne and ground-based radar measurements. *J. Appl. Meteor.*, **39**(12), 2080–2102.

Hou, A. Y., and Coauthors, 2014: The global precipitation measurement mission. *Bull. Amer. Meteor. Soc.*, **95**(5), 701–722.

Houze, R. A., Jr., 1997: Stratiform precipitation in regions of convection: A meteorological paradox? *Bull. Amer. Meteor. Soc.*, **78**(10), 2179–2196.

Houze, R. A., Jr., M. I. Biggerstaff, S. A. Rutledge, and B. F. Smull, 1989: Interpretation of Doppler weather radar displays of midlatitude mesoscale convective systems. *Bull. Amer. Meteor. Soc.*, **70**(6), 608–619.

Houze, R. A., Jr., S. Brodzik, C. Schumacher, S. E. Yuter, and C. R. Williams, 2004: Uncertainties in oceanic radar rain maps at Kwajalein and implications for satellite validation. *J. Appl. Meteor.*, **43**(8), 1114–1132.

Houze, R. A., Jr., D. C. Wilton, and B. F. Smull, 2007: Monsoon convection in the Himalayan region as seen by the TRMM Precipitation Radar. *Quart. J. Roy. Meteor. Soc.*, **133**(627), 1389–1411.

Iguchi, T., T. Kozu, R. Meneghini, J. Awaka, and K. Okamoto, 2000: Rain-profiling algorithm for the TRMM precipitation radar. *J. Appl. Meteor.*, **39**(12), 2038–2052.

Kawanishi, T., and Coauthors, 2000: TRMM precipitation radar. *Advances in Space Research*, **25**(5), 969–972.

Kessinger, C., S. Ellis, J. V. Andel, J. Yee, and J. Hubbert, 2003: The AP clutter mitigation scheme for the WSR-88D. *Preprints, 31st Conference on Radar Meteorology*, Seattle, WA, Amer. Meteor. Soc., 526–529.

Kozu, T., and T. Iguchi, 1999: Nonuniform beamfilling correction for spaceborne radar rainfall measurement: implications from TOGA COARE radar data analysis. *J. Atmos. Oceanic Technol.*, **16**(11), 1722–1735.

Kummerow, C., W. Barnes, T. Kozu, J. Shiue, and J. Simpson, 1998: The tropical rainfall measuring mission (TRMM) sensor package. *J. Atmos. Oceanic Technol.*, **15**(3), 809–817.

Langston, C., J. Zhang, and K. Howard, 2007: Four-dimensional dynamic radar mosaic. *J. Atmos. Oceanic Technol.*, **24**, 776–790.

Liao, L., R. Meneghini, and T. Iguchi, 2001: Comparisons of rain rate and reflectivity factor derived from the TRMM precipitation radar and the WSR-88D over the Melbourne, Florida, site. *J. Atmos. Oceanic Technol.*, **18**(12), 1959–1974.

Liu, L. P., Q. Xu, P. F. Zhang, and S. Liu, 2008: Automated detection of contaminated radar image pixels in mountain areas. *Adv. Atmos. Sci.*, **25**(5), 778–790, doi: 10.1007/s00376-008-0778-x.

Luo, Y. L., Y. J. Wang, H. Y. Wang, Y. J. Zheng, and H. Morrison, 2010: Modeling convective-stratiform precipitation processes on a Mei-Yu front with the Weather Research and Forecasting model: Comparison with observations and sensitivity to cloud microphysics parameterizations. *J. Geophys. Res.*, **115**, D18117, doi: 10.1029/2010JD013873.

Luo, Y. L., W. M. Qian, R. H. Zhang, and D.-L. Zhang, 2013a: Gridded hourly precipitation analysis from high-density rain gauge network over the Yangtze-Huai Rivers Basin during the 2007 Mei-Yu season and comparison with CMORPH. *J. Hydrometeor.*, **14**(4), 1243–1258.

Luo, Y. L., H. Wang, R. H. Zhang, W. M. Qian, and Z. Z. Luo, 2013b: Comparison of rainfall characteristics and convective properties of monsoon precipitation systems over South China and the Yangtze and Huai River basin. *J. Climate*, **26**(1), 110–132.

Luo, Y. L., Y. Gong, and D.-L. Zhang, 2014: Initiation and organizational modes of an extreme-rain-producing mesoscale convective system along a Mei-Yu Front in East China. *Mon. Wea. Rev*, **142**(1), 203–221.

Meng, Z. Y., and Y. J. Zhang, 2012: On the squall lines preceding landfalling tropical cyclones in China. *Mon. Wea. Rev*, **140**(2), 445–470.

Parker, M. D., and R. H. Johnson, 2000: Organizational modes of midlatitude mesoscale convective systems. *Mon. Wea. Rev*, **128**(10), 3413–3436.

Schumacher, C., and R. A. Houze Jr., 2000: Comparison of radar data from the TRMM satellite and Kwajalein oceanic validation site. *J. Appl. Meteor.*, **39**(12), 2151–2164.

Schumacher, R. S., and R. H. Johnson, 2005: Organization and environmental properties of extreme-rain-producing mesoscale convective systems. *Mon. Wea. Rev.*, **133**(4), 961–976.

Schumacher, R. S., and R. H. Johnson, 2006: Characteristics of U.S. extreme rain events during 1999–2003. *Wea. Forecasting*, **21**(1), 69–85.

Simpson, J., C. Kummerow, W.-K. Tao, and R. F. Adler, 1996: On the tropical rainfall measuring mission (TRMM). *Meteor. Atmos. Phys.*, **60**(1–3), 19–36.

Steiner, M., R. A. Houze Jr., and S. E. Yuter, 1995: Climatological characterization of three-dimensional storm structure from operational radar and rain gauge data. *J. Appl. Meteor.*, **34**(9), 1978–2007.

Takahashi, N., H. Kuroiwa, and T. Kawanishi, 2003: Four-year result of external calibration for Precipitation Radar (PR) of the Tropical Rainfall Measuring Mission (TRMM) satellite. *IEEE Transactions on Geoscience and Remote Sensing*, **41**(10), 2398–2403.

TRMM PR Team, 2011: Tropical Rainfall Measuring Mission (TRMM) precipitation radar algorithm Instruction Manual for Version 7. JAXA-NASA, 170 pp. [Available online at http://www.eorc.jaxa.jp/TRMM/documents/PR_algorithm_product_information/pr_manual/PR_Instruction_Manual_V7_L1.pdf.]

Wang, H. Y., L. P. Liu, G. L. Wang, W. Zhuang, Z. Q. Zhang, and X. L. Chen, 2009: Development and application of the Doppler weather radar 3-D digital mosaic system. *Journal of Applied Meteorological Science*, **20**(2), 241–224. (in Chinese)

Wang, J. X., and D. B. Wolff, 2009: Comparisons of reflectivities from the TRMM precipitation radar and ground-based radars. *J. Atmos. Oceanic Technol.*, **26**(5), 857–875.

Xu, W. X., E. J. Zipser, and C. T. Liu, 2009: Rainfall characteristics and convective properties of mei-yu precipitation systems

over South China, Taiwan, and the South China Sea. Part I: TRMM observations. *Mon. Wea. Rev.*, **137**(12), 4261–4275.

Zhang, D.-L., and K. Gao, 1989: Numerical simulation of an intense squall line during 10-11 June 1985 PRE-STORM. Part II: Rear inflow, surface pressure perturbations and stratiform precipitation. *Mon. Wea. Rev.*, **117**, 2067–2094.

Zhang, J., K. Howard, and J. J. Gourley, 2005: Constructing three-dimensional multiple-radar reflectivity mosaics: Examples of convective storms and stratiform rain echoes. *J. Atmos. Oceanic. Technol.*, **22**, 30–42.

Zhao, S. X., L. S. Zhang, and J. H. Sun, 2007: Study of heavy rainfall and related mesoscale systems causing severe flood in Huaihe River basin during the summer of 2007. *Climatic and Environmental Research*, **12**(6), 713–727. (in Chinese)

Zhu, Y. Q., Z. H. Wang, N. Li, F. Xu, J. Han, Z. G. Chu, H. Y. Zhang, and P. C. Jiao, 2016: Consistency analysis and correction for observations from the radar at Nanjing. *Acta Meteorologica Sinica*, **74**(2), 298–308. (in Chinese)

Zipser, E. J., and K. R. Lutz, 1994: The vertical profile of radar reflectivity of convective cells: A strong indicator of storm intensity and lightning probability? *Mon. Wea. Rev.*, **122**(8), 1751–1759.